

New insight into the 24 January 2020, M_w 6.8 Elazığ earthquake (Turkey): An evidence for rupture-parallel pull-apart basin activation along the East Anatolian Fault Zone constrained by Geodetic and Seismological data

Tahir Serkan Irmak^{*,1}, Mustafa Toker², Evrim Yavuz³, Erman Şentürk⁴, Muhammed Ali Güvenaltın⁴

⁽¹⁾ Department of Geophysical Engineering, Kocaeli University, Kocaeli, Turkey

⁽²⁾ Department of Geophysical Engineering, Yüzüncü Yıl University, Van, Turkey

⁽³⁾ İstanbul Metropolitan Municipality, Directorate of Earthquake and Geotechnical Investigation, İstanbul, Turkey

⁽⁴⁾ Department of Geomatics Engineering, Kocaeli University, Kocaeli, Turkey

Article history: received February 8, 2021; accepted June 16, 2021

Abstract

In this study, we investigated the main features of the causative fault of the 24 January 2020, M_w 6.8 Elazığ earthquake (Turkey) using seismological and geodetic data sets to provide new insight into the East Anatolian Fault Zone (EAFZ). We first constrained the co-seismic surface deformation and the rupture geometry of the causative fault segment using Interferometric Synthetic Aperture Radar (InSAR) interferograms (Sentinel-1A/B satellites) and teleseismic waveform inversion, respectively. Also, we determined the centroid moment tensor (CMT) solutions of focal mechanisms of the 27 aftershocks using the regional waveform inversion method. Finally, we evaluated the co-seismic slip distribution and the CMT solutions of the causative fault as well as of adjacent segments using the 27 focal solutions of the aftershocks, superimposed on the surface deformation pattern. The CMT solution of the 24 January 2020 Elazığ earthquake reveals a pure strike-slip focal mechanism, consistent with the structural pattern and left-lateral motion of the EAFZ. The rupture process of the Elazığ event indicated that the rupture is started at 12 km around the hypocenter, and then propagated bilaterally along the NE-SW but mainly toward the southwest. The rupture slip has initially propagated toward the southwest (first 10 s) and northeast (4 s), and again toward the southwest (9 s). Maximum displacement is calculated as 1.3 m about 20 km southwest of the hypocenter at 6 km depth (centroid depth). The rupture stopped to down-dip around 20 km depth toward the southwest. The distribution of the slip vectors indicates that the rupture continued mostly through a normal oblique movement. Most of the moment release was released SW of the hypocenter and the rupture reached up to around 50 km. The focal mechanisms of analyzed 27 aftershocks show strike-slip, but mostly normal and normal oblique-slip faulting with an orientation of the tensional axes (NNE-SSW), indicating a normal oblique-slip, “transtensional” stress regime, parallel-subparallel to the strike of the EAFZ, consistent with SW-rupture directivity and co-seismic deformation pattern. Finally, based on the co-seismic surface deformation compatible

with the distributional pattern of normal focal solutions, normal and normal oblique-slip focals of the aftershocks evidence the rupture-parallel pull-apart basin activation as a segment boundary of the left-lateral strike-slip movement of the EAFZ.

Keywords: East Anatolia; Pull-apart basin activation; Surface deformation; Waveform inversion.

1. Introduction

The NE- and SW-striking East Anatolian Fault Zone (EAFZ) is inter-continental transform fault boundary between Central Anatolian High Plateau (CAP), where the lithospheric mantle separated from the crust and Arabian plate, where lithospheric mantle attached to the crust [Bartol and Govers, 2014] (Figure 1). The left-lateral strike-slip motion of the EAFZ [McClusky et al., 2000; Reilinger et al., 2006; Angus et al., 2006] is the actual boundary between the Arabian and CAP, underneath which the deep Arabian lithosphere is not observable [Angus et al., 2006]. Similar to right-lateral strike-slip faulting in N, the North Anatolian Fault Zone (NAFZ), the EAFZ possesses almost all the characteristics of the thick plate- (Arabian plate in S) and thin plateau- (CAP in N) bounded left-lateral strike-slip faulting and related high earthquake potential (Figure 1). Hence, the EAFZ is a major structural element in the active tectonics of the CAP and the partitioning system of the Eurasia-Arabia collision and thus, accommodates both lateral and also vertical components of oblique convergence in the region [e.g., Lyberis et al., 1992].

The CAP uplifted by the mantle [e.g., Aldanmaz et al., 2000; Ilbeyli et al., 2004; Bartol and Govers, 2014] is underlain by an anomalously thin lithospheric mantle as shown by low seismic wave velocities at sub-crustal levels [Al-Lazki et al., 2004; Gans et al., 2009; Gök et al., 2003; Hearn and Ni, 1994; Maggi and Priestley, 2005; Mutlu and Karabulut, 2011; Schivardi and Morelli, 2011; Bartol and Govers, 2014] and is characterized by a high surface heat flow today [Tezcan and Turgay, 1989; Bartol and Govers, 2014]. A single delamination event modulated by crustal thickening in the continental collision segment of the plate boundary [Bartol and Govers, 2014] suggests that the EAFZ formed a transform seismogenic boundary. CAP predominantly moves westward relative to Eurasia since the time of the Arabian collision, accommodated along the NAFZ and EAFZ [McKenzie, 1976; Şengör, 1979; Dewey and Şengör, 1979; Şengör et al., 1985; Schildgen et al., 2014]. The westward movement of CAP has localized a significant amount of strain accumulation along the EAFZ [Şengör et al., 2005; Faccenna et al., 2006; Özeren and Holt, 2010] and the NAFZ. Previous studies along with the southern CAP margin point to various multi-phases uplift-downlift mechanisms across the EAFZ, which are accompanied by various-sized earthquakes [Taymaz et al., 1991; Kutoğlu et al., 2016], and mainly resulted from strong strain accumulation along the broad bend of the EAFZ [see Schildgen et al., 2014 for details]. Along the EAFZ and NAFZ, interseismic locking depths inferred from geodetic data (2003 to 2010) indicated that the NAFZ is strongly coupled to depth ranges of up to 20 km; while the EAFZ is coupled to shallow depth ranges of up to 5-10 km [Bletery et al., 2020].

The EAFZ is a young and immature fault system, characterized by multiple and discrete fault traces at upper crustal levels [Türkoğlu et al., 2015] and lies within a cryptic area of Arabia-Eurasia collision, where many discontinuous fault segments can be observed [Westaway and Arger, 2001, Westaway, 2003; Moreno et al., 2011] (see Figure 1). These discrete segments seem to play a significant role in accommodating stress sourced from the collision. However, how exactly these small-scale faults relate to the EAFZ is unknown, but their interaction with such a large scale transform fault motion is key to understand how the westward movement of CAP accommodates the Arabia-Eurasia collision along the EAFZ. This is important to develop and to improve the accuracy of earthquake scenarios considered for future seismic hazards in and along the EAFZ. Except for the large destructive earthquakes in and along EAFZ [e.g., Taymaz et al., 1991; Melgar et al., 2020; Cheloni and Akıncı, 2020; Pousse-Beltran et al., 2020; Taymaz et al., 2021], not so many geophysical studies based on national seismic networks have been carried out for EAFZ. For example, the basic role of this large transform fault system on the accommodation of the Eurasia-Arabia collision is debate and has been recently questioned. Although active thrust-reverse faulting is recorded at the further SSW-portion of the EAFZ between the Taurides and the Arabian plate [e.g., 1975, Ms 6.7 thrust earthquake in Lice by Taymaz et al., 1991], oblique-slip deformations associated with discontinuities of fault

The 24 January 2020, M_w 6.8 Elazığ Earthquake (Turkey)

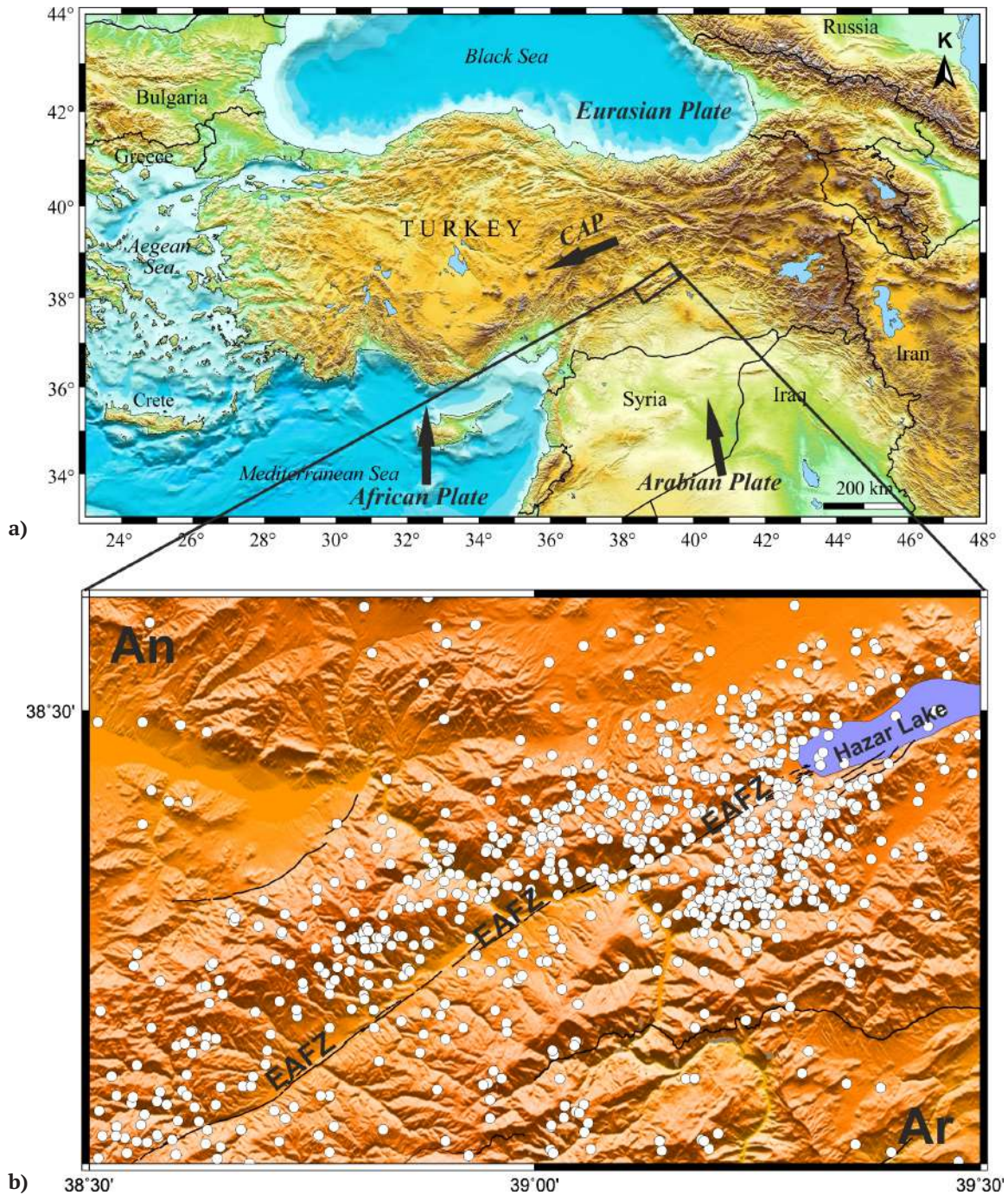


Figure 1. a) Overview of the topography and bathymetry of Turkey and surrounding area. Blue arrows indicate plate motion directions. **An**: Anatolian Plate, **Ar**: Arabian Plate, **CAP**: Central Anatolian High Plateau, **EAFZ**: East Anatolian Fault Zone. b) Epicentral or study area, solid black lines indicate East Anatolian Fault Zone [Duman et al., 2002]. Red star indicates the location of the January 24, 2020 (M_w 6.8) earthquake. White circles indicate the earthquakes larger than 4.0 between 01.01.1900 and 24.02.2020.

segments, parallel-subparallel to the EAFZ, locally exist [e.g., Westaway and Arger, 2001, Westaway, 2003; Moreno et al., 2011]. However, multiple fault traces, parallel-subparallel discrete fault zones, immature structural characteristics, and upper crustal segmentation of the EAFZ [Türkoğlu et al., 2015] have been not constrained yet. Thus, the overall seismotectonic of the EAFZ associated with an orientation of tensional stress (e.g., presence of

normal-slip and normal oblique-slip) in and along the EAFZ is still open. Hence, we feel a strong need for geodetic and seismological information on the EAFZ.

Considering that the NE- and SW-ends of the EAFZ are highly strained sections [Kutoğlu et al., 2016], it is a critical geodynamic setting within the CAP domain where accretionary orogeny is associated with slab delamination and break off in E, and escape tectonics toward W is intricately linked. This interacting plateau domain with a wealth of recent geophysical and geodetic data from CAP and EAFZ that inspired this study spans a wide range of crustal seismic velocity and attenuation tomography studies [e.g., Şahin and Öksüm, 2021 and references therein] and plate model observations [Schildgen et al., 2014; Bartol and Govers, 2014 and references therein] and offers an exceptional chance to understand the seismic potential of EAFZ and evaluate the recently occurred the 24 January 2020, Mw 6.8, Elazığ earthquake in the NE strained section of EAFZ. Although the largest destructive earthquakes were not recorded in the last era in and along the EAFZ [Jamalreyhani et al., 2020], the 24 January 2020 Elazığ mainshock released a seismic moment, accumulated within ~222 years [Bletery et al., 2020; Taymaz et al., 2021].

Source parameters and co-seismic slip distribution of the 24 January 2020 Elazığ mainshock have been studied by extensive research groups, based on strong ground motions and Coulomb stress changes [Cheloni and Akıncı, 2020], geodetic observations [Jamalreyhani et al., 2020; Melgar et al., 2020], moment magnitude and rupture behavior of EAFZ inferred from geodetic data [Pousse-Beltran et al., 2020] and interseismic locking depths of the EAFZ constrained from geodetic observations between years of 2003 and 2010 [Bletery et al., 2020]. In this study, we attempt a better assessment of the deformational relations of the faulting segments (e.g., to Lake Hazar) have remained unknown by using geodetic, earthquake source and aftershock focal mechanisms using near- and far-field approaches. On the other hand, the 24 January 2020 Elazığ mainshock highlights a prominent migration of mainshock-aftershock seismicity, from NE toward SW, along the main fault strike of the EAFZ and possible activations of adjacent oblique fault segments, parallel-subparallel to the EAFZ. Such a characterization of deformation area is, in fact, “unique”, providing an opportunity to understand whether the focal mechanisms constrained by moment tensor solution and teleseismic waveform inversion are consistent with the co-seismic surface displacements and related deformation pattern caused by co-seismic slip of the mainshock in a strike-slip tectonic setting of oblique collision. This is to encourage the current study to perform centroid depths of aftershocks of the Elazığ mainshock using a new approach. The new approach presents the best constraints on both seismological and geodetic data set, particularly in the absence of available near-field recordings.

In this study, we attempt to analyze the co-seismic surface displacements of the 24 January 2020 Elazığ mainshock detected by CORS-TR GNSS stations. At the same time, we examine the source fault ruptured by the mainshock using the horizontal and vertical co-seismic displacement characteristics of the rupturing through analyzing InSAR interferogram images, the co-seismic surface deformations, and pattern of deformational geometry surrounding the rupture area to constrain the source location. Then, we compute teleseismic waveform inversion to obtain co-seismic slip distribution of the source fault rupture and to compare them with co-seismic surface deformations determined by InSAR analyses. Finally, we present the catalog-located aftershock distribution and centroid moment tensor (CMT) solutions of the aftershocks and investigate the deformational compatibility of the co-seismic deformation with co-seismic slip distribution. Our study aims to show evidence for rupture-parallel pull-apart basin activation along the EAFZ using geodetic and teleseismic waveform observations and CMT solutions of aftershocks.

2. Data and Methods

2.1 GNSS and InSAR Data Processing

GNSS observations of 9 stations belonging to the Continuously Operating Reference Stations-Turkey (CORS-TR) Network located around the epicenter of the 24 January 2020 Elazığ earthquake were examined (Figure 2c). The detailed information of stations was given in Table 1. The daily solutions of the stations for 30 days before and after the earthquake were obtained by using GAMIT / GLOBK v.10.73 software [Herring et al., 2015]. Differences in the mean of the solutions obtained from pre-seismic and post-seismic periods were interpreted as the displacement (co-seismic) caused by the earthquake. Also, 1 Hertz observations were analyzed with the GAMIT / Track module. The epicenter distances were correlated with the moments when significant changes occurred in the time series.

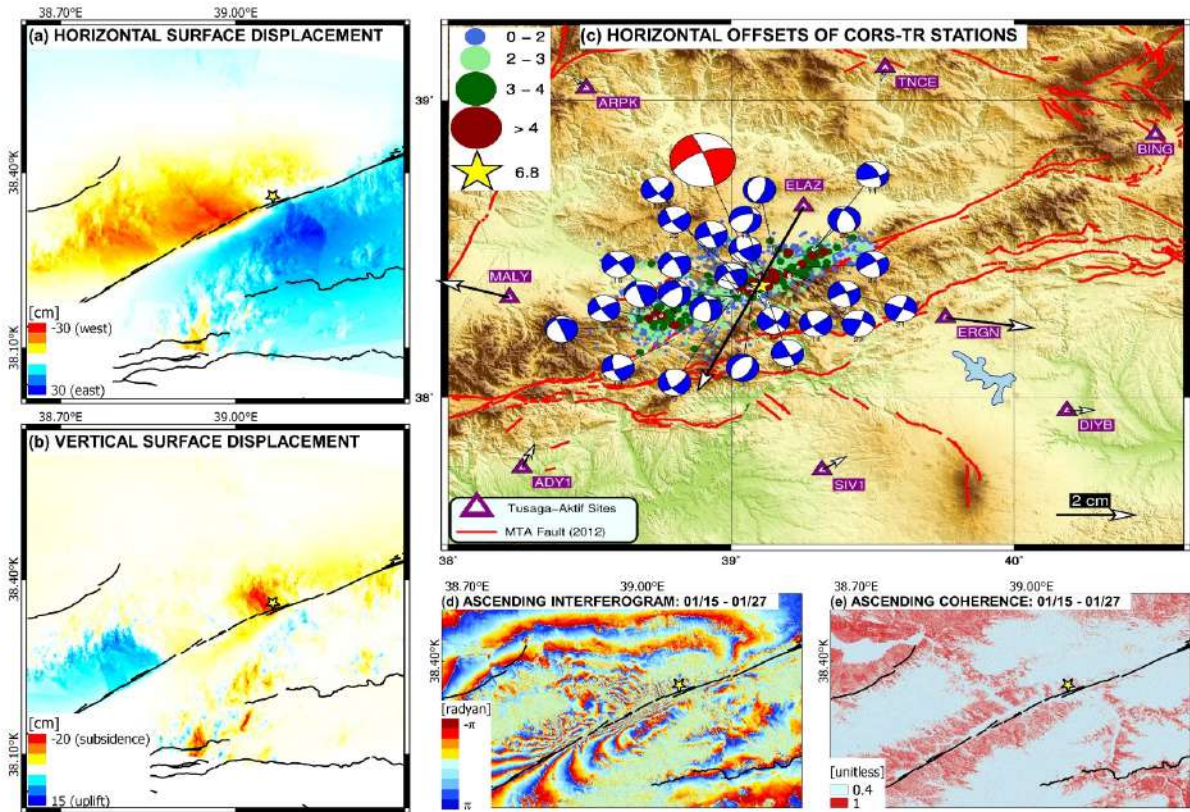


Figure 2. Geodetic observations of the Elazığ earthquake. **a)** Horizontal surface displacements along the rapture zone in E-W direction from InSAR analysis. **b)** Vertical surface displacements. **c)** Velocities of the used CORS-TR stations and focal mechanisms of the mainshock and aftershocks. **d)** Interferogram obtained from master (orbit = 30988, track = 116) and slave (orbit = 30813, track = 116) images in ascending mode. **e)** Coherence map. The solid black and red lines indicate EAFZ. The yellow star shows the epicenter of main event.

STATION CODE	Geog. Coordinates	
	Lat. (N^0)	Long. (E^0)
ADY1	37.7604	38.2612
ARPK	39.0406	38.4873
BING	38.8855	40.5008
DIYB	37.9544	40.1875
ELAZ	38.6447	39.2565
ERGN	38.2696	39.7582
MALY	38.3377	38.2169
SIV1	37.7529	39.3217
TNCE	39.1097	39.5456

Table 1. Detailed information of CORS-TR stations.

We used Sentinel-1 synthetic aperture radar interferometry (InSAR) to monitor the surface deformation produced by the 24 January 2020 Elazığ earthquake. We processed interferometric wide acquisitions from ascending and descending orbits, using open-source SNAP v7.0 ESA software [Veci et al., 2014]. Since they provide a measurement

of ground motion along two opposite lines of sight (LOS), the horizontal and vertical displacements are calculated with the following formulas through the two interferograms [Dalla Via et al., 2012].

$$d_e = \frac{D_d \cos \theta_a - D_a \cos \theta_d}{\sin(\theta_a + \theta_d)} \quad (1)$$

$$d_z = \frac{D_d \sin \theta_a - D_a \sin \theta_d}{\sin(\theta_a + \theta_d)} \quad (2)$$

where θ_a and θ_d , look angles for both orbit modes, D_a and D_d , two displacements measured along the LOS, d_e and d_z , horizontal and vertical components of the displacement, the subscript a and d , ascending and descending, respectively. The parameters of the used ascending and descending image pairs were given in Table 2. In order to calculate displacements in both two orbit modes, we used the digital elevation model (DEM) of SRTM 1 Arc-Second Global for Back Geocoding and Topographic Phase Removal. We also used the Goldstein Phase Filtering [Goldstein and Werner, 1998] with a window size 3 and Fast Fourier Transform size of 128 to enhance the signal to noise ratio (SNR). The interferograms were unwrapped by the statistical-cost, network-flow phase-unwrapping algorithm (SNAPHU) [Chen and Zebker, 2002].

Sr. No.	Slave Image		Master Image		Track	Mode
	Ingestion Date	Orbit	Ingestion Date	Orbit		
1	2020-01-16 T09:57:05.544Z	30820	2020-01-28 T09:48:14.734Z	30995	123	Descending
2	2020-01-15 T19:44:57.093Z	30813	2020-01-27 T18:54:50.341Z	30988	116	Ascending

Table 2. Parameters of the used interferograms.

2.2 Teleseismic Waveform Inversion

In order to estimate a detailed and stable model of the January 24, 2020, Elazığ earthquake, we applied an inversion scheme that was earlier described by Yoshida et al. [1996], Yagi, and Kikuchi [2002], and Yagi et al. [2003]. For this purpose, digital recordings of teleseismic body waveforms for the mainshock, which are clearly visible at 28 seismic stations, were retrieved from Global Seismic Network (GSN).

We assumed that the rupture propagation took place along a single fault. For the discretization of the region to be modeled, we tested different fault dimensions; and then, we finally selected an optimal fault dimension with a total of 27 sub-faults (an area of 10 km x 10 km) consisting of 9 sub-faults in the strike direction and 3 sub-faults in the dip direction. We assumed that the rupture started at the hypocenter. The Green's functions for teleseismic body waves were calculated by using a method of Kikuchi and Kanamori [1991]. In order to represent the region nearby the receiver, we used a standard Jeffreys-Bullen earth model [Jeffreys and Bullen, 1940]. The slip rate function of each sub-fault is expanded into a series of 5 triangle functions with a rise time of 0.6s. The rupture velocity of 3.2 km/s was also selected by trial and error to determine the initiation time of the basis function at each sub-fault.

2.3 Regional Moment Tensor Analysis

In order to obtain the focal mechanism of the aftershocks, we used the ISOLA software which is based on a multiple point source representation [Sokos and Zahradnik, 2008]. The source mechanism is represented by five elementary double-couple sources and one isotropic source as in Kikuchi and Kanamori [1991] and the moment tensor matrix consists of the sum of double-couple (DC) component, compensated linear vector dipole (CLVD), and volumetric (ISO) component (where $DC\% + CLVD\% + ISO\% = 100\%$) [Vavrycuk, 2001]. The Green's functions have been calculated by the discrete wavenumber method of Bouchon [1981]. The quality of the solution is controlled by the variance reduction value which means the highest variance reduction value indicates the best fit between the observed and synthetic waveform. More detailed information for the inversion routine can be found in Sokos and Zahradnik, [2008].

3. Interpretation and discussion

3.1 GNSS and InSAR Analysis

The offsets of the stations indicated significant displacements in the horizontal direction. ELAZ station, which is about 35 km away from the epicenter, slipped around 6 cm in the north-east direction (Figure 2). The ERGN and MALY stations, which are at an average distance of 65 km to the epicenter, moved 3 cm opposite each other in a vertical direction to the fault. The directions of motion of these stations are consistent with the tectonics of the fault. DIYB and SIV1 stations, on the same side as the ERGN but relatively farther away from the fault, have moved in the same direction but at a lower value. The highest deformations in the vertical direction are around 1 cm. Since this value is very close to the standard deviation, it cannot be considered a significant change. Our results coincide with the deformations obtained by Yalvaç [2020] at the mm level.

3.2 Finite Fault Inversion Model

The sequence of aftershocks that is lying in the direction of NE-SW suggests that the rupture also can occur on the fault plane in the NE-SW direction (Figure 3a). Therefore, the finite fault slip modeling was performed for the NE-SW oriented nodal plane. The best solution is shown in Figure 3b. It indicates that major moment release in 20 km southwest of the initiation point of the rupture around the hypocenter with the maximum slip of around 1.30 m at 6 km depth. The obtained seismic moment is 1.815×10^{19} Nm. The rupture duration is about 24 sec. The fitting between 28 observed and synthetic P- waveforms is also shown in Figure 3c. Obtained slip distribution suggests that a main asperity is located around 20 km southwest of the hypocenter or foci. The rupture propagated bilaterally along the NE-SW direction (mainly southwest). Maximum displacement is calculated as 1.3 m about 20 km southwest of the hypocenter at 6 km depth. The rupture stopped to down-dip around 50 km depth toward the southwest. The distribution of the slip vectors indicates that the rupture continued mostly through a normal oblique movement.

3.3 Distributional pattern and focal mechanisms of aftershocks

The regional moment tensor analysis of the analyzed aftershocks is characterized by normal fault and strike-slip faulting with normal faulting component. An example of the analyzed event which is given in Table 3 is shown in Figure 4.

NE-SW trending pattern of aftershock distribution, parallel to the rupture propagation direction toward SW (Figure 3), is characterized by a series of distinct focal mechanisms (Figure 4). The CMT solutions of the aftershocks range from pure strike-slip through normal-oblique-slip to normal-slip within a relatively narrow area of the rupturing process. The centroid depths of the focal mechanisms with normal components are confined at upper crustal depths of up to 10 km (shallow-seated), while those with strike-slip focal mechanisms are started from a

depth of 10 km up to 20 km (deep-seated) (Table 3). Shallow-seated focal depths of events represent thicker sedimentary sections controlled by upper crustal faults, while deep-seated focal depths characterize stable strike-slip motion at middle and/or lower crustal levels.

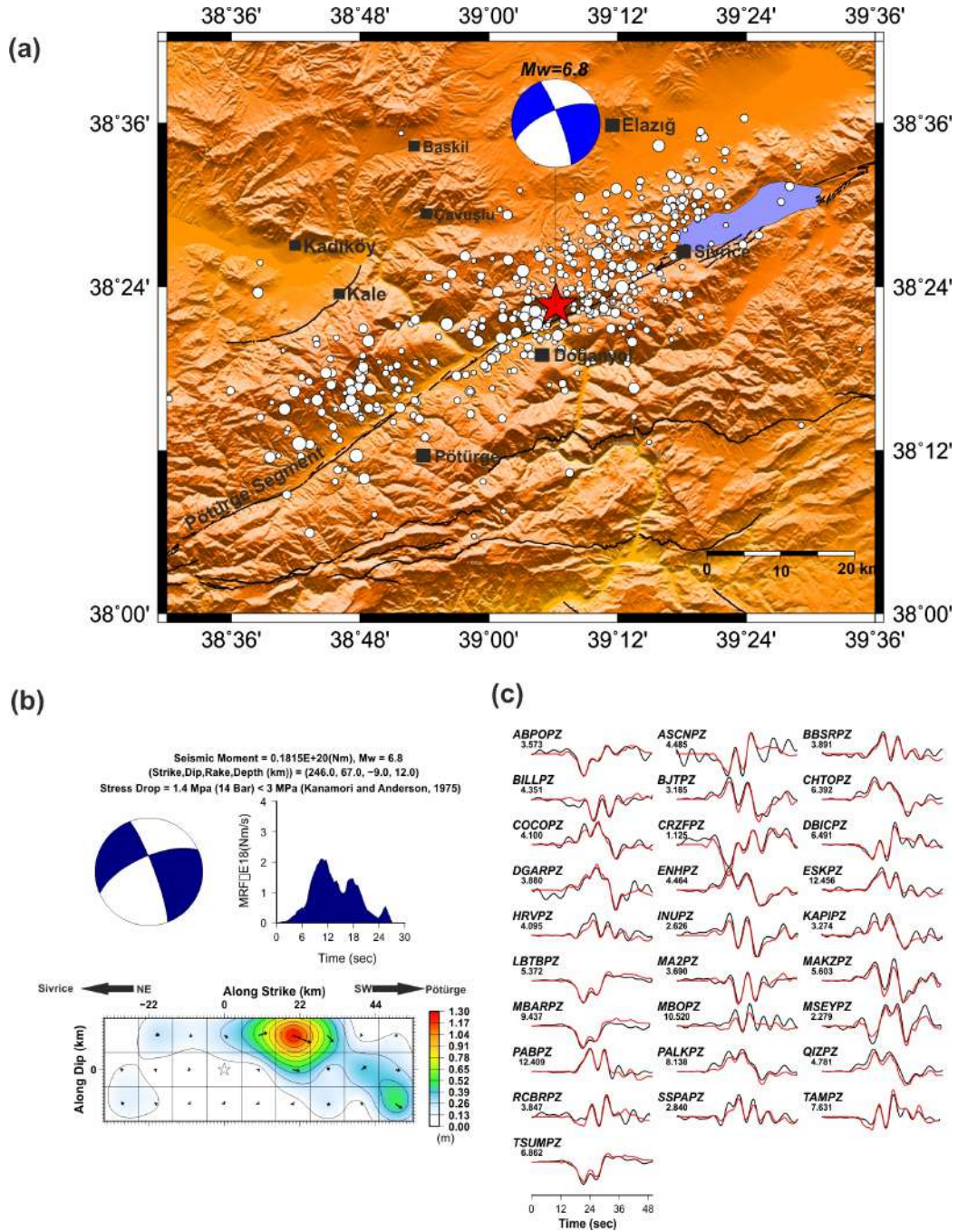


Figure 3. **a)** Epicenter, focal mechanism and 24 hours aftershocks of the 24 January 2020 Elazığ Earthquake, black lines indicate active faults in the study area [Duman et al., 2012]. **b)** Focal mechanism, moment-rate function, co-seismic slip distribution of the 24 January 2020 Elazığ earthquake. The strike, dip and rake angles of the first and second nodal planes (NP), focal depth and seismic moment (M_0) of the earthquake are also given in the header. The white star indicates the focal depth obtained from minimum misfit solution. The vertical scale near the slip model shows the displacement values in meters. **c)** comparison of the observed (black) and synthetic (red) teleseismic broadband P-waveforms used in slip distribution inversion (right). Station code and maximum amplitude are above the waveforms.

The 24 January 2020, M_w 6.8 Elazığ Earthquake (Turkey)

#	Date	OT (UTC)	Lat (°N)	Lon (°E)	CD (km)	SM (Nm)	M_w	Strike (°)	Dip (°)	Rake (°)	DC (%)	CLVD (%)	VR
1	24.01.2020	19:49:37.31	38.4395	39.1692	7.5	3.715×10^{15}	4.3	66/335	88/88	2/178	65.5	34.5	0.50
2	24.01.2020	20:42:10.12	38.3502	39.0780	5.5	6.005×10^{14}	3.8	33/216	49/41	-92/-87	90.6	9.4	0.58
3	24.01.2020	20:45:02.79	38.4227	39.1212	9.5	3.316×10^{15}	4.3	62/153	87/59	-31/-177	90.3	9.7	0.69
4	24.01.2020	22:01:32.82	38.3398	39.0423	10.0	6.719×10^{14}	3.8	359/240	47/63	-141/-50	80.5	19.5	0.76
5	24.01.2020	22:19:28.78	38.3333	38.9845	2.0	2.278×10^{14}	3.5	350/234	65/47	-131/-35	50.4	49.6	0.46
6	25.01.2020	00:48:49.64	38.4763	39.1532	5.5	1.321×10^{15}	4.0	19/180	66/25	-82/-108	82.8	17.2	0.63
7	25.01.2020	00:57:16.81	38.3705	39.0723	6.5	7.325×10^{14}	3.8	239/332	64/85	-5/-154	96.6	3.4	0.69
8	25.01.2020	04:37:56.69	38.3302	39.0017	5.5	4.215×10^{14}	3.7	150/49	61/71	-158/-31	79.1	20.9	0.60
9	25.01.2020	06:07:32.47	38.3703	39.0598	6.0	1.263×10^{15}	4.0	236/335	59/75	-17/-148	94.5	5.5	0.62
10	25.01.2020	08:40:03.23	38.5040	39.3003	12.5	2.405×10^{15}	4.2	73/332	71/61	31/158	82.3	17.7	0.54
11	25.01.2020	10:14:55.73	38.1968	38.8008	8.0	3.246×10^{15}	4.3	71/164	84/66	-24/-173	76.0	24.0	0.69
12	25.01.2020	16:30:07.18	38.3518	39.0263	7.0	2.358×10^{16}	4.8	143/49	79/70	-160/-12	75.3	24.7	0.51
13	25.01.2020	16:44:00.79	38.3662	39.0817	9.5	2.843×10^{15}	4.2	145/53	76/81	-171/-14	83.8	16.2	0.51
14	25.01.2020	16:46:59.08	38.4447	39.0955	5.5	2.231×10^{15}	4.2	15/253	51/57	-135/-49	61.0	39.0	0.59
15	26.01.2020	02:22:45.65	38.2803	38.8103	6.5	3.949×10^{15}	4.3	323/232	82/83	-173/-8	93.8	6.2	0.56
16	26.01.2020	10:12:16.86	38.3423	39.0978	10.5	6.504×10^{14}	3.8	312/42	89/71	161/1	99.1	0.9	0.67
17	26.01.2020	11:31:31.90	38.2670	38.7315	18.5	2.355×10^{14}	3.5	255/160	79/67	23/168	95.7	4.3	0.56
18	27.01.2020	16:11:59.41	38.4078	39.0980	5.5	2.245×10^{15}	4.2	159/69	89/86	-186/-1	84.5	15.5	0.65
19	31.01.2020	23:32:48.96	38.5002	39.2917	8.0	7.051×10^{15}	4.5	324/195	46/57	-131/-56	88.0	12.0	0.70
20	01.02.2020	00:03:48.01	38.4128	39.2070	1.5	1.213×10^{15}	4.0	151/241	87/85	175/3	50.3	49.7	0.71
21	03.02.2020	22:19:39.77	38.3703	39.0773	4.0	4.685×10^{15}	4.4	49/142	85/61	-30/-174	98.1	1.9	0.70
22	07.02.2020	19:57:04.38	38.4032	39.2083	1.5	1.137×10^{15}	4.0	22/288	80/69	21/170	77.6	22.4	0.81
23	17.02.2020	11:42:14.04	38.3222	39.1332	5.5	2.695×10^{15}	4.2	67/335	70/84	6/160	75.2	24.8	0.73
24	25.02.2020	23:03:34.43	38.2767	38.7523	15.0	2.353×10^{16}	4.8	162/257	86/33	123/6	91.9	8.1	0.55
25	27.02.2020	02:08:46.15	38.2392	38.6430	7.0	2.185×10^{15}	4.2	341/238	82/23	-112/-19	99.0	1.0	0.71
26	29.02.2020	12:29:46.03	38.4385	39.2367	2.0	3.601×10^{15}	4.3	240/333	83/65	-25/-172	94.2	5.8	0.75
27	19.03.2020	17:53:30.08	38.3952	39.0948	5.5	3.351×10^{16}	5.0	68/323	69/56	36/155	99.2	0.8	0.64

Table 3. Source parameters of the analyzed aftershocks obtained from regional moment tensor analysis. **OT:** Origin Time, **CD:** Centroid Depth, **SM:** Seismic Moment, **M_w :** Moment Magnitude, **DC:** Double Couple, **CLVD:** Compensated Linear Vector Dipole, **VR:** Variance Reduction.

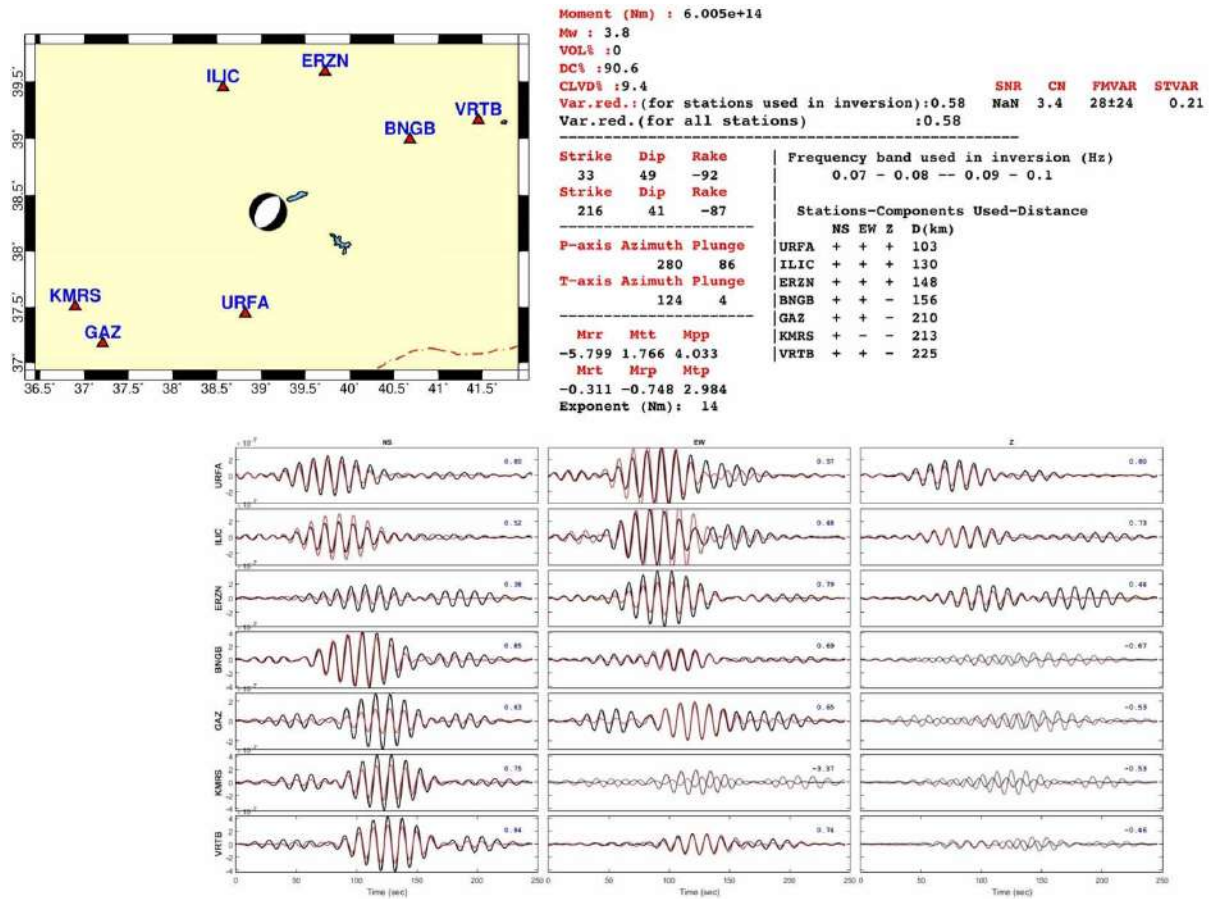


Figure 4. The regional moment tensor analysis result for the event no 2 in Table 3. (Upper). Obtained focal mechanism and source parameters. (Lower) waveform fitting, black: observed seismograms, red: calculated seismograms. Gray traces did not used in inversion process.

The distributional pattern of aftershock seismicity and their focal mechanisms shown in Figure 5 are also correlated with the co-seismic horizontal (Figure 6) and vertical (Figure 7) deformation results obtained from the modeling of InSAR for the Elazığ earthquake. Seismicity pattern of aftershocks shown in Figures 6a and 7a and related focal mechanisms shown in Figures 6b and 7b are well consistent with the horizontal and vertical components of co-seismic deformation. As shown in Figure 2, the same as Figure 7, the vertical displacement ranges from 20 cm (max) to 10 cm (min) within an extended subsidence area toward SW (Anatolian side) parallel to the rupture directivity (Figure 3) compatible with the focals with the normal component. Toward the further SW, a narrowed uplift area parallel to the rupture directivity is ranged from 15 cm (max) to 10 cm (min). Maximum W-E horizontal displacement for deep-seated strike-slip focal is ± 30 cm (Figure 6). In Figures 6 and 7, the seismicity pattern of aftershocks and the focal mechanisms with normal components are also well compatible with patchy-like crushed patterns of butterfly geometry of co-seismic interferogram shown in Figure 2. In Figure 2, through crushed sections, co-seismic coherency sharply decreases to a minimum value of 0.4 and remains stable, suggesting an anomalous vertical surface displacement; widespread down lift and prominent subsidence in the Anatolian side, rather than the uplift localized at SW-end. However, no unexpected anomaly in and along the horizontal surface displacement is observable along crushed sections of butterfly geometry, compatible with deep-seated strike-slip focals.

The comparison of co-seismic deformation obtained from InSAR observations shown in Figure 2 to aftershock seismicity (Figures 6a and 7a) and focal mechanisms (Figures 6b and 7b) reveals that the downlifting, consistent with shallow-seated focal with the normal component, characterizes co-seismic vertical deformation in the Anatolian side, rather than the Arabian side and that the uplifting is only a localized effect in the Anatolian side. However, the W-E horizontal surface displacement (± 30 cm) shows co-seismic surface deformation compatible with deep-seated strike-slip focals, the source mechanism of the mainshock, and the SW directivity of the rupture source (Figure 3).

The 24 January 2020, M_w 6.8 Elazığ Earthquake (Turkey)

It is noticeable from the vertical surface displacement from the extensive down lift to the local uplift, consistent with the rupture directivity from NE to SW, the shallow-seated normal focals, and those with the normal component, that the rupture source started from its initiation point at NE (maximum subsidence and focals with normal components), propagated to the SW (maximum local uplift) strongly deformed the Anatolian side (Figures 6 and 7).

Although the source mechanism and co-seismic slip distribution of the Elazığ mainshock located on the EAFZ indicate left-lateral strike-slip motion (Figure 3) compatible with the horizontal component of co-seismic surface displacement (Figure 2), we interpret that its aftershock sequence is not related only to the activity of the main fault ruptured by the mainshock and that some other controlling discrete faults are segmented in the study area. As indicated in Figures 6b and 7b (also see Figure 5), the focal solutions of the number of aftershocks show different mechanisms, not compatible with a deep and large-scale transform motion of the EAFZ. The shallow-seated focal solutions distinctly show the existence of NE-SW and NNE-SSW oriented tension. This suggests pure normal and also normal oblique-slip faults consistent with the pull-apart mechanism. As given by Figure 7, the vertical component of the co-seismic surface displacement, seismicity pattern of aftershocks, shallow-seated normal focals, and those with normal component confirm, to a certain extent, the presence of pull-apart basin activation that may have been formed due to left lateral shearing of the EAFZ. We consider that this finding is highly matched with the Lake Hazar pull-apart structure [Moreno et al., 2011 and references therein], suggesting possible reactivation of pre-existing normal and/or normal oblique-slip faults that form, bound, and follow the Lake Hazar in the NE [e.g., the Lake Hazar as a result of negative flower structure proposed by Aksoy et al., 2007; Moreno et al., 2011].

Considering the rupture-parallel pull-apart basin activation associated with normal and normal oblique-slip focal mechanisms of shallow-seated aftershocks in the N of the EAFZ (the Anatolian side), the assumption of a simple strike-slip motion on a single main fault is unlikely to be correct due to crustal diversity and misfits of focal mechanisms caused by rupture source complexity in and along EAFZ. Pull-apart basin activation controlled by discontinuous fault segments within the ruptured area is in good agreement with the results obtained from the crustal-scale observations along the EAFZ [e.g., low seismic velocity by Gans et al., 2009; very low electrical resistivity by Türkoğlu et al., 2015; low velocity-high attenuation by Şahin and Öksüm, 2021] but surprisingly, has not been constrained by early studies [e.g., Melgar et al., 2020; Cheloni and Akıncı, 2020; Pousse-Beltran et al., 2020; Bletery et al., 2020; Jamalreyhani et al., 2020].

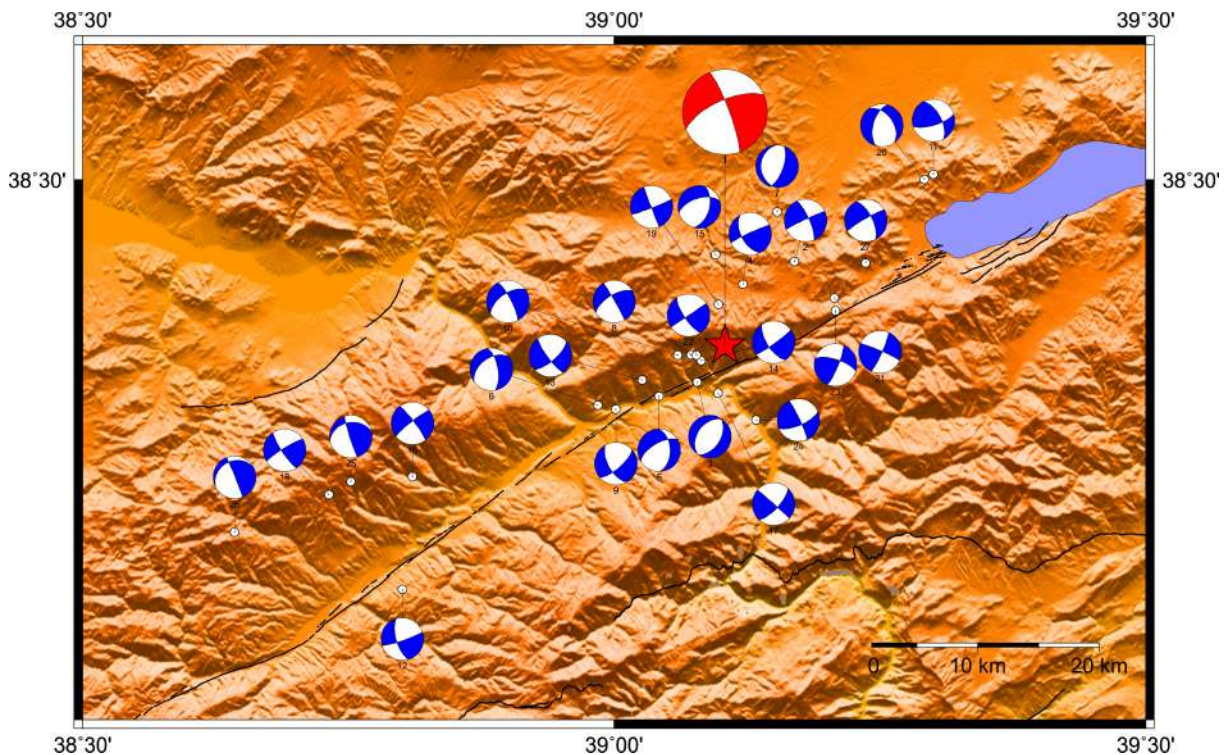


Figure 5. Focal mechanism of the analysed aftershocks in the study area.

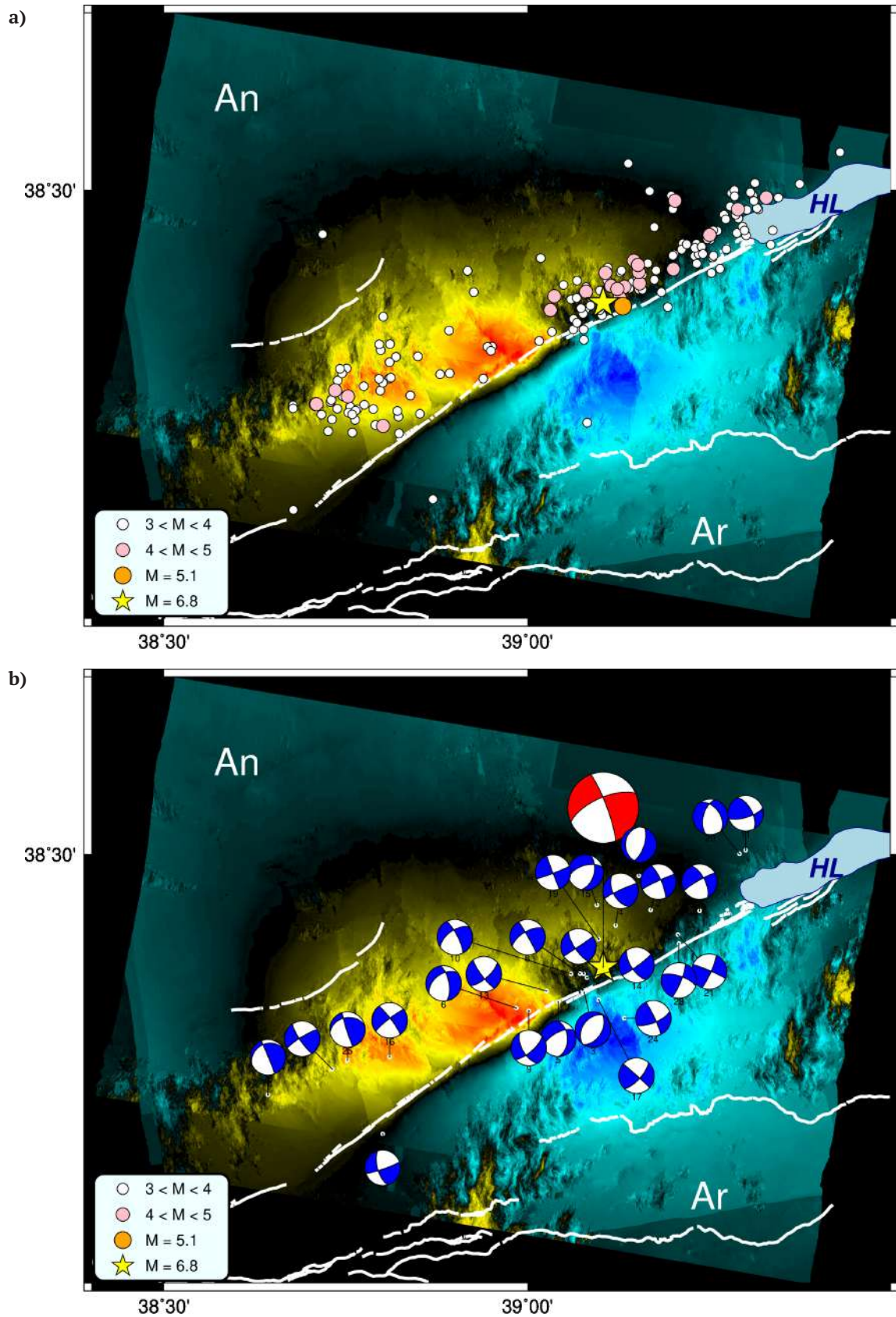


Figure 6. The epicentre of the 2020 Elazığ mainshock, distribution of aftershocks and their focal mechanisms superimposed on the horizontal component of the co-seismic surface displacement shown in Figure 2a. **a)** Seismicity pattern of aftershocks, and **b)** their focal mechanisms. Beach ball in red indicates the mainshock (An: Anatolian Block, Ar: Arabian Plate, HL: Hazar Lake).

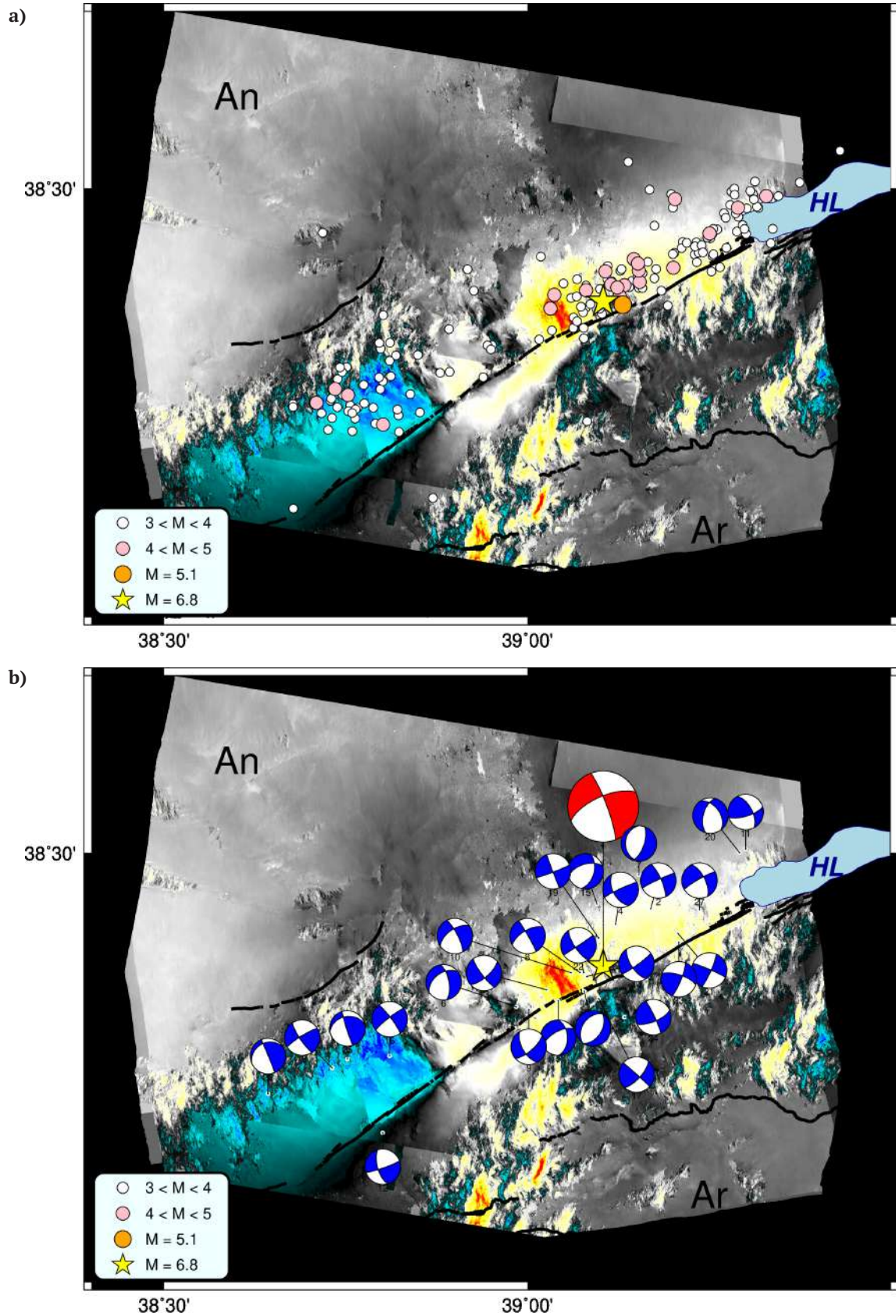


Figure 7. The epicentre of the 2020 Elazığ mainshock, distribution of aftershocks and their focal mechanisms superimposed on the vertical component of the co-seismic surface displacement shown in Figure 2b. **a)** Seismicity pattern of aftershocks, and **b)** their focal mechanisms. Beach ball in red indicates the mainshock (An: Anatolian Block, Ar: Arabian Plate, HL: Hazar Lake).

5. Conclusions

The rupture process of the 24 January 2020 Elazığ Earthquake indicates major moment release in 20 km southwest of the hypocenter with the maximum slip of around 1.30 m at 6 km depth. The main asperity is located around 20 km southwest of the hypocenter. The rupture propagated bilaterally along the NE-SW direction (mainly southwest). The rupture stopped to down-dip around 20 km depth toward the southwest from the hypocenter.

The average centroid depths of the analyzed aftershocks with the normal component are shallower (~10 km) than those with strike components and also elsewhere in the EAFZ. Except for the left-lateral strike-slip focal mechanism of the 24 January 2020 Elazığ mainshock, there are two main trends of aftershocks for which estimated focal mechanisms are dominantly normal components, implying extensional and transtensional movements parallel to SW-rupture propagation in the Anatolian side. The co-seismic vertical surface deformation supports the proposed existence of the normal component and rupture-parallel pull-apart mechanism, close to Lake Hazar in the further NE.

The 24 January 2020 Elazığ mainshock-aftershock sequence is one of the most important earthquakes controlling and driving the westward extrusion tectonics of the CAP along the EAFZ. The focal mechanisms and the co-seismic surface deformation, particularly its vertical component are observed to have strongly localized in thin crustal CAP in N (the Anatolian side), rather than the thick lithospheric Arabian plate in S (the Arabian side). Normal-slip and normal oblique-slip aftershock focal mechanisms support and confirm the strain partitioning of the Eurasia-Arabia collision along the EAFZ and thus, the EAFZ accommodates both lateral and also vertical components of oblique convergence in the region. Finally, the study of the 2020 Elazığ earthquake concludes that the westward movement of the CAP is accommodated by not only the left-lateral strike-slip motion of EAFZ but also the upper crustal extensional-transtensional motions in and along EAFZ.

Acknowledgments. The authors are grateful to the organizations including the General Directorate of Mapping, General Directorate of Land Registry and Cadastre, the International GNSS Service, the EUREF Permanent Network for GNSS data, and the Research and Service Support team of the European Space Agency (ESA) for InSAR data. The authors send their greatest thanks to Prof. Dr. Ali Pinar (Boğaziçi University, Kandilli Observatory, and Earthquake Research Institute, Turkey) for his comments on waveform fits on normal focal solutions and also appreciate Dr. Yuji Yagi for providing the slip inversion code. The authors acknowledge the Kocaeli University Research Fund and Disaster and Emergency Management Presidency of Turkey (AFAD) for providing computing facilities. This study was partially supported by AFAD (Project Number: AFAD-G-20-07).

References

- Aksoy, E., M. Inceoz and A. Kocyigit (2007). Lake Hazar Basin: a negative flower structure on the East Anatolian Fault System (EAFS), SE-Turkey, *Turkish J. Earth Sci.*, 16, 319-338.
- Aldanmaz, E., J.A. Pearce, M.F. Thirlwall and J.G. Mitchell (2000). Petrogenetic evolution of late Cenozoic, post-collision volcanism in western Anatolia, Turkey, *J. Volcanol. Geotherm. Res.*, 102, 1-2, 67-95.
- Al-Lazki, A.I., E. Sandvol, D. Seber, M. Barazangi, N. Turkelli and R. Mohamad (2004). Pn tomographic imaging of mantle lid velocity and anisotropy at the junction of the Arabian, Eurasian and African plates, *Geophys. J. Int.*, 158(3), 1024-1040.
- Angus, D.A., D.C. Wilson, E. Sandvol and J.F. Ni (2006). Lithospheric structure of the Arabian and Eurasian collision zone in eastern Turkey from S-wave receiver functions, *Geophys. J. Int.*, 166, 1335-1346.
- Bartol, J. and R. Govers (2014). A single cause for uplift of the Central and Eastern Anatolian plateau? *Tectonophysics*, 637, 116-136.
- Bleter, Q., O. Cavalié, J.M. Nocquet and T. Ragon (2020). Distribution of interseismic coupling along the North and East Anatolian Faults inferred from InSAR and GPS data. *Geophys. Res. Lett.*, 47, 16, e2020GL087775, <https://doi.org/10.1029/2020GL087775>.
- Bouchon, M. (1981). A simple method to calculate Green's functions for elastic layered media, *Bulletin of the*

- Seismol. Soc. Am., 71, 4, 959-971.
- Cheloni, D. and A. Akinçi (2020). Source modelling and strong ground motion simulations for the 24 January 2020, M_w 6.8 Elazığ earthquake, Turkey, *Geophys. J. Int.*, 223, 2, 1054-1068.
- Chen, C.W. and H.A. Zebker (2001). Two-dimensional phase unwrapping with use of statistical models for cost functions in nonlinear optimization, *JOSA A*, 18, 2, 338-351.
- Dalla Via, G., M. Crosetto and B. Crippa (2012). Resolving vertical and east-west horizontal motion from differential interferometric synthetic aperture radar: The L'Aquila earthquake, *J. Geophys. Res.*, 117, B02310, <https://doi.org/10.1029/2011JB008689>.
- Dewey, J.F. and A.C. Sengor (1979). Aegean and surrounding regions: complex multiplate and continuum tectonics in a convergent zone, *Geol. Soc. of America Bulletin*, 90, 1, 84-92.
- Duman, T.Y., Ö. Emre, S. Özalp, H. Elmacı and Ş. Olgun (2012). 1: 250.000 Scale Active Fault Map Series of Turkey, Elazığ (NJ 37-7) Quadrangle. Serial Number: 45, General Directorate of Mineral Research and Exploration, Ankara -Turkey.
- Faccenna, C., O. Bellier, J. Martinod, C. Piromallo and V. Regard (2006). Slab detachment beneath eastern Anatolia: A possible cause for the formation of the North Anatolian fault, *Earth Planet. Sci. Lett.*, 242, 1-2, 85-97.
- Gans, C.R., S.L. Beck, G. Zandt, C.B. Biryol and A.A. Özacar (2009). Detecting the limit of slab break-off in central Turkey: new high-resolution Pn tomography results, *Geophys. J. Int.*, 179, 3, 1566-1572.
- Gök, R., E. Sandvol, N. Türkelli, D. Seber and M. Barazangi (2003). Sn attenuation in the Anatolian and Iranian plateau and surrounding regions, *Geophys. Res. Lett.*, 30, 24, <https://doi.org/10.1029/2003GL018020>.
- Goldstein, R.M. and C.L. Werner (1998). Radar interferogram filtering for geophysical applications, *Geophys. Res. Lett.*, 25, 21, 4035-4038.
- Hearn, T.M. and J.F. Ni (1994). Pn velocities beneath continental collision zones: the Turkish-Iranian Plateau, *Geophys. J. Int.*, 117, 2, 273-283.
- Herring, T.A., R.W. King and S.C. McClusky (2015). Introduction to GAMIT/GLOBK 10.6. Mass. Inst. of Tech., Cambridge.
- İlbeyli N., J.A. Pearce, M.F. Thirlwall and J.G. Mitchell (2004). Petrogenesis of collision-related plutonics in Central Anatolia, Turkey, *Lithos*, 72, 3-4, 163-182.
- Jamalreyhani, M., P. Büyükakpınar, S. Cesca, T. Dahm, H. Sudhaus, M. Rezapour, M.P. Isken, B. Maleki Asayesh and S. Heimann (2020). Seismicity related to the eastern sector of Anatolian escape tectonic: the example of the 24 January 2020 M_w 6.77 Elazığ-Sivrice earthquake, *Solid Earth Discussions*, 1-22, <https://doi.org/10.5194/se-2020-55>.
- Jeffreys, H. and K.E. Bullen (1940). Seismological tables, British Association Seismological Committee, London.
- Kikuchi, M. and H. Kanamori (1991). Inversion of complex body waves - III, *Bull. Seismol. Soc. Am.*, 81, 6, 2335-2350.
- Kutoğlu, H.S., M. Toker and C. Mekik (2016). The 3-D strain patterns in Turkey using geodetic velocity fields from the RTK-CORS (TR) network. *J. African Earth Sci.*, 115, 246-270.
- Lyberis, N.T., T. Yurur, J. Chorowicz, E. Kasapoglu, and N. Gundogdu (1992). The East Anatolian Fault: an oblique collisional belt, *Tectonophysics*, 204, 1-15.
- Maggi, A. and K. Priestley (2005). Surface waveform tomography of the Turkish-Iranian plateau, *Geophys. J. Int.*, 160, 3, 1068-1080.
- McClusky, S., S. Balassanian, A. Barka, C. Demir, S. Ergintav, I. Georgiev, O. Gurkan, M. Hamburger, K. Hurst, H. Kahle, K. Kastens, G. Kekelidze, R. King, V. Kotzev, O. Lenk, S. Mahmoud, A. Mishin, M. Nadariya, A. Ouzounis, D. Paradissis, Y. Peter, M. Prilepin, R. Reilinger, I. Sanlı, H. Seeger, A. Tealeb, M.N. Toksöz and G. Veis (2000) GPS constraints on plate motion and deformation in the eastern Mediterranean: implication for plate dynamics, *J. Geophys. Res.*, 105, 5695-5719.
- McKenzie, D. (1976). The East Anatolian Fault: a major structure in eastern Turkey. *Earth Planet. Sci. Lett.*, 29, 1, 189-193.
- Melgar, D., A. Ganas, T. Taymaz, S. Valkaniotis, B.W. Crowell, V. Kapetanidis, V. Tsironi, S. Yolsal-Çevikbilen and T. Öcalan (2020). Rupture kinematics of 2020 January 24 M_w 6.7 Doğanyol-Sivrice, Turkey earthquake on the East Anatolian Fault Zone imaged by space geodesy, *Geophys. J. Int.*, 223, 2, 862-874.
- Moreno, D., A. Hubert-Ferrari, J. Moernaut, J.G. Fraser, X. Boes, M. Van Daele, U. Avsar, N. Cagatay and M. De

- Batist (2011). Structure and recent evolution of the Hazar basin: A strike-slip basin on the East Anatolian fault, eastern Turkey, *Basin Res.*, 23, 2, 191-207.
- Mutlu, A.K. and H. Karabulut (2011). Anisotropic Pn tomography of Turkey and adjacent regions, *Geophys. J. Int.*, 187, 3, 1743-1758.
- Özeren, M.S. and W.E. Holt (2010). The dynamics of the eastern Mediterranean and eastern Turkey, *Geophys. J. Int.*, 183, 3, 1165-1184.
- Pousse-Beltran, L., E. Nissen, E.A. Bergman, M.D. Cambaz, É. Gaudreau, E. Karasözen and F. Tan (2020). The 2020 Mw 6.8 Elazığ (Turkey) earthquake reveals rupture behavior of the East Anatolian Fault. *Geophys. Res. Lett.*, 47, e2020GL088136, <https://doi.org/10.1029/2020GL088136>.
- Reilinger, R., S. McClusky, P. Vernant, S. Lawrence, S. Ergintav, R. Cakmak, H. Ozener, F. Kadirov, I. Guliev, R. Stepanyan, M. Nadariya, G. Hahubia, S. Mahmoud, K. Sakr, A. ArRajehi, D. Paradissis, A. Al-Aydrus, M. Prilepin, T. Guseva, E. Evren, A. Dmitrotsa, S.V. Filikov, F. Gomez, R. Al-Ghazzi and G. Karam (2006). GPS constraints on continental deformation in the Africa-Arabia-Eurasia continental collision zone and implications for the dynamics of plate interactions. *J. Geophys. Res.*, 111, B05411, <https://doi.org/10.1029/2005JB004051>.
- Şahin, Ş. and E. Öksüm (2021). The Relation of Seismic Velocity and Attenuation Pattern in the East Anatolian Fault Zone with Earthquake Occurrence: Example of January 24, 2020 Sivrice Earthquake, *Bull. Min. Res. Exp.*, 165-191.
- Schildgen, T.F., C. Yıldırım, D. Cosentino and M.R. Strecker (2014). Linking slab break-off, Hellenic trench retreat, and uplift of the Central and Eastern Anatolian plateaus, *Earth-Sci. Rev.*, 128, 147-168.
- Schivardi, R. and A. Morelli (2011). EPMantle: a 3-D transversely isotropic model of the upper mantle under the European Plate, *Geophys. J. Int.*, 185, 1, 469-484.
- Sengör, A.M.C. (1979). The North Anatolian transform fault: its age, offset and tectonic significance, *J. Geol. Soc.*, 136, 3, 269-282.
- Şengör, A.M.C., N. Görür and F. Şaroğlu (1985). Strike-slip faulting and related basin formation in zones of tectonic escape: Turkey as a case study. *SEPM Soc. Sediment, Geol.*, 37, 227-264.
- Şengör, A.M.C., O. Tüysüz, C. Imren, M. Sakınç, H. Eyidoğan, N. Görür, X. Le Pichon and C. Rangin (2005). The North Anatolian fault: A new look, *Annu. Rev. Earth Planet. Sci.*, 33, 37-112.
- Sokos, E.N. and J. Zahradnik (2008). ISOLA a Fortran code and a Matlab GUI to perform multiple-point source inversion of seismic data, *Compu. Geosci.*, 34, 8, 967-977.
- Taymaz, T., H. Eyidoğan and J. Jackson (1991). Source parameters of large earthquakes in the East Anatolian Fault Zone (Turkey), *Geophys. J. Int.*, 106, 537-550.
- Taymaz, T., A. Ganas, S. Yolsal-Çevikbilen, F. Vera, T. Eken, C. Erman, D. Keleş, V. Kapetanidis, S. Valkaniotis, I. Karasante and V. Tsironi (2021). Source Mechanism and Rupture Process of the 24 January 2020 Mw 6.7 Doğanyol–Sivrice Earthquake obtained from Seismological Waveform Analysis and Space Geodetic Observations on the East Anatolian Fault Zone (Turkey), *Tectonophysics*, 228745.
- Tezcan A.K. and I. Turgay (1989). Heat flow map of Turkey. General Directorate of Mineral Research and Exploration (MTA), Department of Geophysics Research, Ankara (in Turkish, unpublished).
- Türkoğlu, E., M. Unsworth, F. Bulut and İ. Çağlar (2015). Crustal structure of the North Anatolian and East Anatolian Fault Systems from magnetotelluric data. *Phys. Earth Planet. Inter.*, 241, 1-14.
- Vavryčuk, V. (2001). Inversion for parameters of tensile earthquakes. *J. Geophys. Res.*, 106, 16339-16355.
- Veci, L., J. Lu, P. Prats-Iraola, R. Scheiber, F. Collard, N. Fomferra and M. Engdahl (2014). The Sentinel-1 Toolbox in Proceedings of the IEEE International Geoscience and Remote Sensing Symposium (IGARSS), 1-3. IEEE.
- Westaway, R. (2003). Kinematics of the Middle East and Eastern Mediterranean Updated, *Turkish J. Earth Sci.*, 12, 5-56.
- Westaway, R. and J. Arger (2001) Kinematics of the Malatya–Ovacik Fault Zone, *Geodinam. Acta*, 14, 103-131.
- Yagi, Y. and M. Kikuchi (2002). Partitioning between seismogenic and aseismic slip as highlighted from slow slip events in Hyuga-nada, Japan, *Geophys. Res. Lett.*, 30, 2.
- Yagi, Y., M. Kikuchi and T. Nishimura (2003). Co-seismic slip, post-seismic slip, and largest aftershock associated with the 1994 Sanriku-haruka-oki, Japan, earthquake, *Geophys. Res. Lett.*, 30, 22, <https://doi.org/10.1029/2003GL018189>.
- Yalvaç, S. (2020). Determining the Effects of the 2020 Elazığ-Sivrice/Turkey (Mw 6.7) Earthquake from the

The 24 January 2020, M_w 6.8 Elazığ Earthquake (Turkey)

Surrounding CORS-TR GNSS Stations, Turkish J. Geosci., 1, 1, 15-21.

Yoshida, S., K. Koketsu, B. Shibasaki, T. Sagiya, T. Kato and Y. Yoshida (1996). Joint inversion of near- and far-field waveforms and geodetic data for the rupture process of the 1995 Kobe earthquake, J. Phys. Earth, 44, 437-454.

***CORRESPONDING AUTHOR: Tahir SERKAN IRMAK**

Department of Geophysical Engineering,

Kocaeli University, Kocaeli, Turkey,

e-mail: irmakts@kocaeli.edu.tr

© 2021 the Author(s). All rights reserved.

Open Access. This article is licensed under a Creative Commons Attribution 3.0 International

The 24 January 2020, M_w 6.8 Elazığ Earthquake (Turkey)

